Optics & Laser Technology 192 (2025) 113398

Contents lists available at ScienceDirect

Optics and Laser Technology

journal homepage: www.elsevier.com/locate/jolt

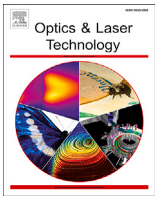

Full length article

Silicon slot metasurface supporting a multitude of bound states in the continuum: theoretical and experimental studies

G. Nousios[a,*], J.F. Algorri[b,c,d], W. Fuscaldo[a], F. Dell'Olio[e], S. Romano[f], G. Zito[f], B. Miranda[f], Y. Ding[g,h], V. Dmitriev[i], L.C. Andreani[j], M. Galli[j], O. Tsilipakos[k], E.E. Kriezis[l], D.C. Zografopoulos[l,a]

[a] Consiglio Nazionale delle Ricerche, Istituto per la Microelettronica e Microsistemi (CNR-IMM), Rome, 00133, Italy
[b] Photonics Engineering Group, University of Cantabria, Santander, 39005, Spain
[c] CIBER-bbn, Instituto de Salud Carlos III, Madrid, 28029, Spain
[d] Instituto de Investigación Sanitaria Valdecilla (IDIVAL), Santander, 39011, Spain
[e] Department of Electrical and Information Engineering, Polytecnic University of Bari, Bari, 70125, Italy
[f] CNR ISASI Institute of Applied Sciences and Intelligent Systems, Naples, 80078, Italy
[g] SiPhotonIC ApS, Virum Stationsvej 207, Virum, 2830, Denmark
[h] Department of Electrical and Photonics Engineering, Technical University of Denmark, Ørsteds Plads, Bygning 343, Kongens Lyngby, 2800, Denmark
[i] Electrical Engineering Department, Federal University of Pará, Belém, 66075-900, Brazil
[j] Dipartimento di Fisica, Università di Pavia, Pavia, 27100, Italy
[k] Theoretical and Physical Chemistry Institute, National Hellenic Research Foundation, Athens, GR-11635, Greece
[l] School of Electrical and Computer Engineering, Aristotle University of Thessaloniki (AUTH), Thessaloniki, GR-54124, Greece

HIGHLIGHTS

- Silicon slot metasurface supporting a rich variety of bound states in the continuum.
- The modal properties are accurately extracted through eigenfrequency simulations.
- Multipole expansion reveals the near- and the far-field properties of the modes.
- Experimental measurements confirming the existence of the investigated modes.
- The metasurface serves as an ideal platform for lasing and nonlinear applications.

ARTICLE INFO

Keywords:
Silicon metasurfaces
Bound states in the continuum
Nanofabrication
Multipole analysis
Metasurface lasers
Nonlinear nanophotonics

ABSTRACT

A dielectric metasurface supporting a variety of quasi-bound states in the continuum (qBICs), including the intricate dark toroidal dipole and toroidal quadrupole Mie modes, is theoretically and experimentally investigated in the near-infrared. The metasurface consists of square slots etched into a thin silicon layer and periodically arrayed in a subdiffractive lattice residing on a sapphire substrate. The modal properties of the qBICs, i.e., the quality factors alongside the near- and far-field characteristics, are comprehensively assessed through a set of theoretical tools, including eigenfrequency simulations and multipolar expansion analysis. The results are corroborated by experimental studies verifying the existence of the qBICs. The investigated metasurface may serve as an ideal platform for nonlinear applications, such as third-harmonic generation, when leveraging the Kerr effect of silicon, as well as for lasing when the slot is filled with a low-index material hosting organic dye molecules.

1. Introduction

Metasurfaces have gathered immense scientific attention during the last decade for applications spanning almost the entire electromagnetic spectrum, from microwaves to the visible [1]. More specifically, all-dielectric metasurfaces, consisting of transparent and high refractive-index nanoresonators arrayed in subdiffractive lattices,

---

[*] Corresponding author.
Email address: georgios.nousios@artov.imm.cnr.it (G. Nousios).

https://doi.org/10.1016/j.optlastec.2025.113398
Received 10 March 2025; Received in revised form 12 June 2025; Accepted 13 June 2025

are particularly attractive as they interact strongly with incident electromagnetic waves and support an abundance of resonances, including electric, magnetic, and toroidal Mie multipoles, as well as surface-lattice resonances (SLRs) [2–4]. Additionally, dielectric metasurfaces do not suffer from the ohmic losses of their plasmonic counterparts. Appropriately designed dielectric metasurfaces have already been exploited for advanced-functionality applications, such as reconfigurable wavefront manipulation [5], refractometric sensing [6], optical filtering [7], passive radiative cooling [8], spatial light modulation [9], and nonreciprocal elements [10].

The emergence of dielectric metasurfaces hosting bound states in the continuum (BICs), i.e., nonradiative (dark) modes that lie within but are uncoupled from the radiation continuum, has opened new avenues for a wide range of applications [11–17]. As they are decoupled from radiation fields, BICs are characterized by infinite radiative quality factors (in the infinite periodic system), whereas their total quality factor is limited only by losses related to material absorption and fabrication imperfections. For the BICs to interact with impinging waves, however, they have to be transformed into quasi-BICs (qBICs) which can controllably couple to radiation fields and have finite radiative quality factors. In the most commonly investigated case of symmetry-protected BICs, this is achieved by appropriately introducing structural asymmetries in the metasurface structure [18]. Along with high quality factors, qBIC-metasurfaces offer intense near-field enhancement and strong light confinement at the nanoscale, hence boosting the light-matter interaction and enabling lasing and the manifestation of nonlinear effects. In particular, silicon qBIC-metasurfaces have already been realized for third- (THG) [19–22] and higher- (HHG) harmonic generation up to the eleventh order [23], by harnessing the strong Kerr effect in silicon. In those configurations, a light beam in the mid- or near-infrared is exploited to parametrically generate a wave in the visible or ultraviolet (UV) region. Degenerate four-wave mixing (DFWM) has also been demonstrated in Refs. [22,23]. Even more interesting is the exploitation of qBIC-metasurfaces for lasing applications. A number of novel works have already been published and diverse gain media have been exploited, such as semiconductors [24], colloidal nanoplatelet quantum wells [25], and organic dye solutions [26–29], thus, paving the way for low-threshold ultrathin lasing structures.

Motivated by the aforementioned developments, in this work we theoretically and experimentally study a subdiffractive square slot metasurface based on the silicon-on-sapphire platform. Mesh-type metasurfaces comprising narrow slots etched in thin silicon layers and forming split-rings or -squares have recently been proposed and studied to some extent in Refs. [6,30,31]. This work complements and expands the existing literature as outlined below. The metasurface under study supports a variety of BIC states in the wavelength region 1300–2000 nm with distinct field profiles. Such rich variety of physical resonances makes the investigated metasurface an excellent platform for highly efficient nonlinear applications when harnessing the Kerr effect in silicon, as well as for optically pumped lasing when the slot is filled by a low-index polymer hosting organic dye molecules. To facilitate the coupling of the supported BICs to radiation fields, the symmetry of the metasurface is reduced by introducing a thin silicon bridge splitting the square slots. The modal properties of the supported qBICs, such as resonance wavelengths, quality factors, and field profiles, are accurately evaluated through finite element method (FEM) simulations utilizing an augmented- or auxiliary-fields eigenfrequency formulation, which allows for the explicit consideration of the dispersive properties of the underlying materials [32,33]. The nature of the supported qBICs in terms of Mie multipoles is assessed by performing multipolar expansion analysis [34]. The latter study also reveals the mechanism behind the transformation of the dark states into quasi-dark ones and, consequently, the far-field properties of the supported qBICs are obtained. To corroborate the theoretical studies, we have fabricated the examined metasurface through electron-beam lithography (EBL) followed by inductively coupled plasma (ICP) etching. The existence of the qBICs is experimentally confirmed by measuring the transmission spectrum under normally incident excitation.

The rest of the paper is organized as follows: In Section 2 the modal properties of the supported qBICs are theoretically evaluated, followed by the experimental studies in Section 3. In Section 4 the suitability of each of the investigated qBICs for nonlinear and lasing applications is thoroughly discussed. Finally, Section 5 offers concluding remarks.

2. Bright and dark Mie resonances in square-slotted silicon metasurfaces

2.1. Physical structure

The metasurface under study is depicted in Fig. 1. It consists of periodically arrayed square slots etched in a thin silicon layer of thickness $h = 200$ nm and residing on top of a semi-infinite sapphire substrate. The geometric parameters of the unit cell have been carefully selected for the metasurface to support a variety of qBICs with distinct modal properties in an extended wavelength range spanning from 1300 nm to 2000 nm. In particular, the inner seperation of slots is $w = 710$ nm, the distance between adjacent squares $g = 50$ nm, while the slot width is $s = 40$ nm. Hence, the pitch of the metasurface is $\Lambda = w + 2\ s + g = 840$ nm. The symmetry of the unit cell is reduced by a thin silicon bridge of width t splitting the square slots along the y axis, as shown in Fig. 1. This symmetry reduction facilitates the transformation of the supported BICs to qBICs with finite quality factors (see below). In the considered spectral range, the relative permittivity of silicon is accurately given by a single-pole Drude–Lorentz relation reading $\varepsilon_{r,\mathrm{Si}} = 1 - \omega_p^2\left(\omega^2 - \omega_0^2 - j\omega\gamma\right)^{-1}$, where $\omega_p = 2.0405\ \times 10^{16}$ rad/s and $\omega_0 = 6.2472 \times 10^{15}$ rad/s are the plasma and resonance frequencies, respectively. The damping coefficient is set to $\gamma = 0$ as silicon is transparent in the considered wavelength range from 1300 nm to 2000 nm. Nonetheless, a non-zero value of γ could be used to take into account fabrication-quality-related imperfections that introduce scattering and/or absorption losses. Note also that for $\gamma = 0$ the considered Drude–Lorentz relation coincides with the standard Sellmeier equation of silicon, when only the dominant term is retained. Sapphire, on the other hand, is considered to be dispersionless (and lossless) with a constant refractive index of $n_s = 1.74$. Given the value of the pitch and the refractive index of the substrate, it is straightforward to determine that the metasurface is subdiffractive for wavelengths $\lambda > n_s\Lambda = 1461.6$ nm, assuming a normally incident plane wave.

2.2. Eigenvalue and multipolar expansion analysis

Initially, the optical modes of the symmetric metasurface ($t = 0$) are studied. To this end, we conduct eigenfrequency simulations with the unit cell of the metasurface using the commercially available COMSOL Multiphysics® software that implements vectorial FEM. The lateral sides of the unit cell are terminated by appropriate periodic boundary conditions, whereas vertically the computational domain is truncated by

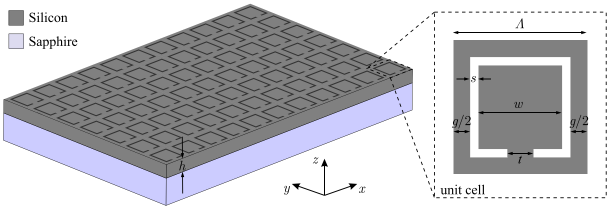

Fig. 1. 3D schematic illustration of the considered metasurface comprised of periodically arranged square slots fully etched in a silicon layer of thickness h. The structure resides on a semi-infinite sapphire substrate. The symmetry of the metasurface is broken by a silicon bridge of width t splitting the square slots along the y axis. Inset: Unit cell of the metasurface on the xy-plane depicting the geometric parameters of the structure.

Table 1
Resonance wavelengths λ_0 and quality factors Q of the supported modes in the symmetric and asymmetric metasurface.

Modes	Symmetric ($t = 0$)		Asymmetric ($t = 60$ nm)	
	λ_0 (nm)	Q	λ_0 (nm)	Q
B_1	1348.24	50	1375.81	80
D_1	1480.66	∞	1484.26	3796
B_2[a]	1517.16	59	1517.63	59
	1517.23	59	1521.88	69
D_2	1547.64	∞	1550.72	76236
D_3	1555.02	∞	1555.75	122533
D_4	1737.14	∞	1737.61	8×10^7
B_3[a]	1827.74	800	1831.79	894
	1827.78	804	1838.62	434
D_5	1957.19	∞	1957.78	$\sim 10^7$

[a] Two degenerate resonances in the symmetric metasurface. Any difference in the values of λ_0 and Q concerning the two degenerate resonances is due to numerical error.

perfectly matched layers (PMLs). To accurately consider silicon's dispersion in the eigenfrequency evaluations, we exploit the augmented- or auxiliary-fields formulation of Ref. [32], which can be appropriately embedded in the eigenfrequency module of COMSOL Multiphysics®. The necessity behind the use of this formulation stems from the fact that material dispersion renders the eigenvalue problem nonlinear. This would mean that an iterative approach is essential for the accurate extraction of the resonance frequency, while the precise calculation of the quality factor is challenging and could require extensive post-processing with the evaluated eigenvectors, especially in the case of leaky modes [35–37]. With the auxiliary-fields formulation, on the other hand, the dispersive optical properties of the underlying cavity materials are explicitly considered through a number of independent polarization and current fields following typical Drude–Lorentz relations. The number of auxiliary fields is twice the number of the Drude–Lorentz poles that are necessary for the accurate description of each material's optical properties. Subsequently, the auxiliary-field equations accompanied by Maxwell's curl equations define a linear eigenvalue problem through which the modal properties (resonance frequency, quality factor, and modal profile) are accurately evaluated. In this study, we focus on investigating the eigenstates of the metasurface that can be excited by a normally incident plane wave in the $\pm\hat{\mathbf{z}}$ direction.

The resonance wavelengths λ_0 and the quality factors Q of the supported modes when $t = 0$ are summarized in Table 1. Note that the presented quality factors are solely describing radiative losses, since the underlying materials are lossless. The metasurface hosts three bright Mie modes with low radiative quality factors which are marked as B_i with $i = \{1, 2, 3\}$; "B" stands for bright. Each of the modes B_2 and B_3 comprises essentially two degenerate resonances with identical resonance wavelengths and quality factors; the small difference in their λ_0 and Q values presented in Table 1 is attributed to numerical error. However, their field distributions are orthogonal to each other, meaning that each degenerate resonance can only be coupled to incident light of a specific polarization (in the x and y direction, respectively) [31]. Apart from the bright modes, the metasurface under examination also supports five dark Mie modes marked as D_i with $i = \{1, 2, 3, 4, 5\}$; "D" stands for dark. These modes constitute symmetry-protected BICs, which are completely decoupled from the radiation fields in the normal direction and characterized by infinite radiative quality factors. Note that a BIC would acquire a finite-valued radiative quality factor if its resonance wavelength is lower than the diffraction limit [24]. In that case the quality factor describes the radiation losses attributed to the coupling of the BIC to propagating higher-order diffraction fields. This, however, is not the case here since the resonance wavelengths of all five BICs are greater than the onset of the first diffraction order ($\lambda_0 > n_s\Lambda = 1461.6$ nm). For the rest of this work, we exclusively focus on the study of the BICs D_1, D_2, D_3, and D_4.

The field distribution of the four BICs at the $z = 0$ plane (middle of the silicon layer) are presented in Fig. 2(a–d), respectively. The respective field profiles at the $x = \Lambda/4$ plane [marked with a gray dashed line in Fig. 2(a–d)] are illustrated in Fig. 2(e–i). Color portrays the norm of the electric field, while the black (red) arrows refer to the electric (magnetic) field. The four BICs are characterized by substantially different field profiles, with the modes D_1, D_2, D_3 equally confined in both silicon and slot areas, while the BIC D_4 is a slot mode. The field distributions can also provide an indication of each mode's order, e.g., dipole, quadrupole. For instance, the four electric-field loops with alternating direction of erasure arranged in pairs in the xy-plane [Fig. 2(a)] along with the perpendicularly circulating magnetic field in the yz-plane [Fig. 2(e)], indicate that the mode D_1 is a toroidal quadrupole. To undoubtedly deduce the nature of the four modes we perform a multipole expansion in the polarization current distributions of the eigenvectors using the expressions of Ref. [34]. For the evaluation of the multipole moments, we use the eigenvectors extracted in the absence of the sapphire substrate, thus, eliminating any ambiguity regarding the integration volume that may be introduced in the presence of the semi-infinite substrate. Then, each moment is multiplied by an appropriate factor to acquire the corresponding contribution to the scattered field [see Eq. (10) in Ref. [34]]. The latter allows for the direct comparison of different-order multipole terms with each other, which otherwise would be inconsistent. The results are compiled in Fig. 2(j–m) for the four BICs under examination. The electric, magnetic, and toroidal dipole components are marked as p_j, m_j, and T_j, respectively, while the electric, magnetic, and toroidal quadrupole tensor components as $Q^{(e)}_{jk}$, $Q^{(m)}_{jk}$, and $Q^{(T)}_{jk}$, respectively. Also, the components of the electric and magnetic octupole tensors are denoted as $O^{(e)}_{jk\ell}$ and $O^{(m)}_{jk\ell}$, respectively, where $\{j, k, \ell\} = \{x, y, z\}$. Consequently, we can confirm that the mode D_1 is of toroidal quadrupole nature, as the dominant moments are the $Q^{(T)}_{xx}$ and $Q^{(T)}_{yy}$ [Fig. 2(j)]. The mode D_2, on the contrary, is characterized by a dominant $Q^{(m)}_{xy}$ moment [Fig. 2(k)] rendering it a magnetic quadrupole. Similarly, the modes D_3 and D_4 are recognized as toroidal dipole and electric quadrupole, respectively, since their corresponding dominants moments are the T_z [Fig. 2(l)] and $Q^{(e)}_{xy}$ [Fig. 2(m)]. These conclusions are also in complete accordance with the mode profiles in Fig. 2. It is also noteworthy that all presented moments in Fig. 2(j–m) are dark, meaning that they do not radiate in the far-field in the normal direction. The magnitude of other dark moments, such as the out-of-plane magnetic dipole m_z, is negligible in comparison with those presented in Fig. 2(j–m). We also refer to Ref. [31] for a comprehensive study of the supported BICs from the perspective of symmetry through a rigorous mathematical analysis based on group theory and the symmetry adapted linear combination (SALC) method.

In Fig. 3(a) and (b) we additionally present the resonance wavelengths and the radiative quality factors, respectively, of the BICs D_1, D_2, D_3, and D_4 along part of the $\Gamma \rightarrow \mathrm{M}$ ($k_x = 0 - \pi/\Lambda$, $k_y = 0$) and $\Gamma \rightarrow \mathrm{X}$ ($k_x = k_y = 0 - \pi/\Lambda$) directions of the first Brillouin zone of the symmetric ($t = 0$) metasurface; k_i is the i-component of the Floquet/Bloch wavenumber with $i = \{x, y\}$. The evaluations have been conducted through eigenfrequency simulations with COMSOL Multiphysics®. This study reveals the properties of the investigated eigenstates when the metasurface is illuminated at an oblique direction, which are important for many practical nonlinear and lasing applications. Along the $\Gamma \rightarrow \mathrm{M}$ direction, the modes D_1 and D_2 exhibit only mild dispersion of their resonance wavelengths, in contrast to modes D_3 and D_4. On the other hand, along the $\Gamma \rightarrow \mathrm{X}$ direction all of the examined modes are characterized by significant dispersion of their resonance wavelengths, except for D_1 around the Γ point. In addition, the discontinuity of the λ_0 curve for the mode D_1 at $k_x \approx 0.1\pi/\Lambda$ along the $\Gamma \rightarrow \mathrm{M}$ direction is attributed to Wood's anomaly (WA), as higher-order diffraction modes become propagating. Similarly for the mode D_1 at $k_x \approx 0.08\pi/\Lambda$, as well as for D_3 and D_4 at $k_x \approx 0.21\pi/\Lambda$ along the $\Gamma \rightarrow \mathrm{X}$ direction. Notably the abrupt decrease of the quality factors from infinite to finite values around the Γ point indicates once more that the examined dark resonances are symmetry-protected BICs.

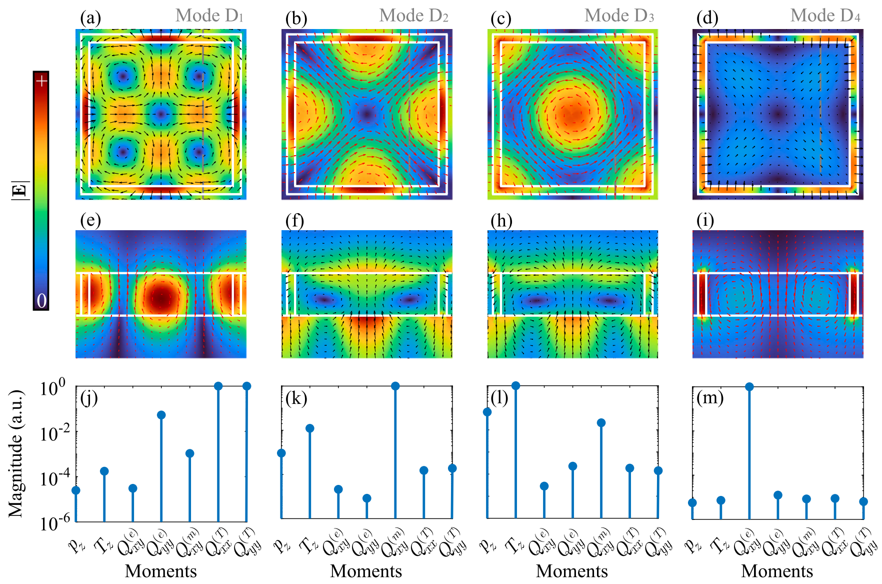

Fig. 2. Eigenvalue analysis of the BICs D_1, D_2, D_3, and D_4 of the symmetric ($t = 0$) metasurface. (a–i) Field plots at the (a–d) $z = 0$ (middle of the silicon layer), and (e–i) $x = \Lambda/4$ [gray dashed line in Fig. 2(a–d)] planes for the four considered BICs, respectively. The colormaps portray the norm of the electric field (linear scale), while the black and red arrows depict the electric and magnetic fields, respectively. (j–m) Multipolar expansion in the polarization currents of the eigenvector of the four BICs, revealing the nature of the investigated modes. The eigenvectors considered for the multipolar expansion have been evaluated in the absence of the substrate.

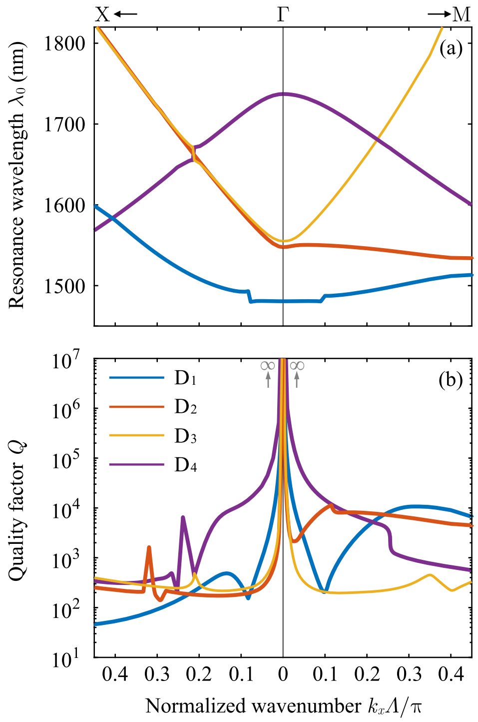

Fig. 3. (a) Resonance wavelengths λ_0, and (b) radiative quality factors Q of the BICs D_1, D_2, D_3, and D_4 along the $\Gamma \rightarrow$ M and $\Gamma \rightarrow$ X directions of the first Brillouin zone for the symmetric ($t = 0$) metasurface.

As already explained, the previously studied BICs cannot be coupled to radiation fields in the normal direction, prohibiting their exploitation in practical nonlinear and lasing applications. Therefore, a silicon bridge is introduced to reduce the symmetry of the metasurface, transforming the BICs into qBICs with finite yet very high quality factors. In Table 1 we compile the resonance wavelengths and radiative quality factors of the supported modes when $t = 60$ nm (asymmetric metasurface). All the dark modes now acquire finite quality factors, although their values range from few thousands (D_1) to tens of millions (D_4). This is due to the fact that the introduction of the silicon bridge affects differently each mode. In particular, the modes D_1, D_2, and D_3 have strong electric field concentration in the area where the asymmetry is introduced [see Fig. 2(a–c)], hence their field distributions and, consequently, their quality factors are greatly perturbed by the silicon bridge. On the other hand, the electric field distribution of the mode D_4 is almost zero in the vicinity of the bridge [Fig. 2(d)], resulting only in a small change of its modal properties. The dependence of the quality factors of the qBICs D_1, D_2, D_3, and D_4 on the width t of the silicon bridge is presented in Fig. 4. For lower values of t (i.e., the silicon bridge is a small perturbation), all the Q curves follow the established inverse quadratic law for nondiffracting metasurfaces [38]. This behavior changes, however, for higher values of t. Notably the radiative quality factor of D_2 exhibits a local maximum for $t \approx 200$ nm which is attributed to the formation of an accidental BIC (A-BIC) [17], as thoroughly explained in Ref. [31]. As also highlighted previously, the qBIC D_4 requires much higher values of t in order to achieve a quality factor in the tens of thousands in contrast to the modes D_1, D_2, and D_3. Nonetheless, it is evident that the desired value of the radiative quality factor can always be achieved for

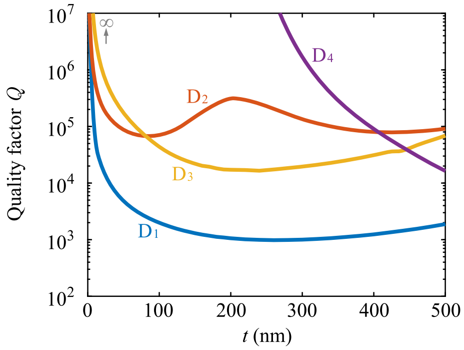

Fig. 4. Radiative quality factor of the qBICs D_1, D_2, D_3, and D_4 as a function of the width t of the silicon bridge.

all four of the examined qBICs by appropriately tuning the width of the silicon bridge. In addition, the degeneracy of the bright modes B_2 and B_3 is lifted in the asymmetric metasurface, as the presence of the silicon bridge affects differently the field profiles of the two initially degenerate resonances.

The transformation of the dark modes to quasi-dark ones as the symmetry of the metasurface is reduced, can be unraveled by performing multipole expansion analysis with the polarization currents of the eigenvectors in the asymmetric metasurface ($t = 60$ nm); once again the evaluations are conducted in the absence of the sapphire substrate. In principle, symmetry breaking enables the mixing of the dark multipole term or moment that characterizes each BIC, with bright moments, which are then coupled to radiation fields in the normal direction [18]. The four modes under investigation can be separated in two distinct groups. In the first group we have the qBICs D_1, D_2, and D_3, which can only be coupled to radiation fields in the normal direction that are polarized in the y direction. The second group comprises of the qBIC D_4 (and D_5), which is only coupled to radiation fields polarized in the x direction. The separation of the investigated modes in two different groups stems from the specific symmetry reduction that the silicon bridge introduces in the metasurface's unit cell, as it can be rigorously deduced by a mathematical analysis based on group theory and the SALC method [31]. Alternatively, one can reach the same conclusions through the multipolar expansion analysis (see below).

We initially study the modes of the first group (D_1, D_2, and D_3). The bright moments which are excited by normally incident light polarized in the y direction and scatter light in the normal direction and with the same polarization, are the p_y, m_x, T_y, $Q_{yz}^{(e)}$, $Q_{xz}^{(m)}$, and $O_{yzz}^{(e)}$ [34]; the moments $Q_{yz}^{(T)}$ and $O_{xzz}^{(m)}$ also belong to this category but their influence was found negligible for all three modes and, hence, they are omitted. Subsequently, in Fig. 5(a) we present the magnitude of the previously mentioned bright moments for the mode D_1 when $t = 0$ (blue circles) and $t = 60$ nm (red squares), respectively. Each moment's magnitude has been normalized with respect to the magnitude of the dominant dark moment $Q_{xx}^{(T)}$ (or equivalently $Q_{yy}^{(T)}$), which as explained previously does not radiate in the far-field in the normal direction. Note that the small values the magnitude of the bright moments receive in the symmetric structure are solely attributed to the inherent limitations associated with the numerical calculation, as introduced by the discretization of the computational domain. Thus, the shaded area in Fig. 5(a) denotes a practically zero level for the bright moments' magnitude. The introduction of the silicon bridge leaves unaffected the dominant moment and, hence, the nature of the mode. Nonetheless, it results in an almost three orders of magnitude increase for the moments p_y, T_y, $Q_{xz}^{(m)}$, and $O_{yzz}^{(e)}$. However, caution is required as some combinations of these moments can nullify one another [39]. This is exactly the case with the mode D_1 as the moments T_y, $Q_{xz}^{(m)}$, and $O_{yzz}^{(e)}$ effectively cancel each other out and, as a result, their overall far-field contribution is negligible. This is revealed in Fig. 5(d), where the far-field contribution of each moment individually in terms of the power they scatter in the normal direction, is plotted as a function of the wavelength around the mode D_1, when the asymmetric metasurface is normally excited by a plane wave polarized in the y direction. The multipole moments are now evaluated using the polarization currents generated by the total (incident and scattered) electric field rather than the eigenvector. Note that the resonance wavelength of all modes is substantially shifted in the absence of the sapphire substrate [cf. Table 1]; the modes D_2 and D_3 are affected much more than the mode D_1 due to the substantial overlap of their field profiles with the sapphire substrate [Fig. 2(f) and (h)]. The combined far-field contribution of the moments T_y, $Q_{xz}^{(m)}$, and $O_{yzz}^{(e)}$ is presented with gray curve showcasing their mutual cancellation; the cancellation is not complete though due to inherent limitations associated with the numerical calculation. Thus, only the electric p_y and magnetic m_x dipoles dictate the far-field scattering spectrum in the vicinity of the resonance D_1. Notice that the spectrum of m_x is practically constant without exhibiting a Fano lineshape similar to those of the rest of the moments. This means that the magnetic dipole moment solely captures non-resonant/background contributions. This is fully consistent with Fig. 5(a), which shows that the magnetic dipole m_x remains practically zero with the introduction of the silicon bridge; its small nonzero value is attributed to inherent limitations associated with the numerical calculation, as mentioned previously. This is due to the fact that performing multipole expansion analysis using the polarization currents of the eigenvector reveals only the resonant contributions. It is also noteworthy that in Fig. 5(d) the contribution of $Q_{yz}^{(e)}$ is practically zero in the entire presented spectrum.

The transmission and reflection spectra evaluated by the reconstruction of the scattered field using the combined contribution of all the bright moments presented in Fig. 5(d) [dashed lines in Fig. 6] are identical to those calculated directly through plane-wave scattering simulations with COMSOL Multiphysics® [solid lines in Fig. 6]. Similar

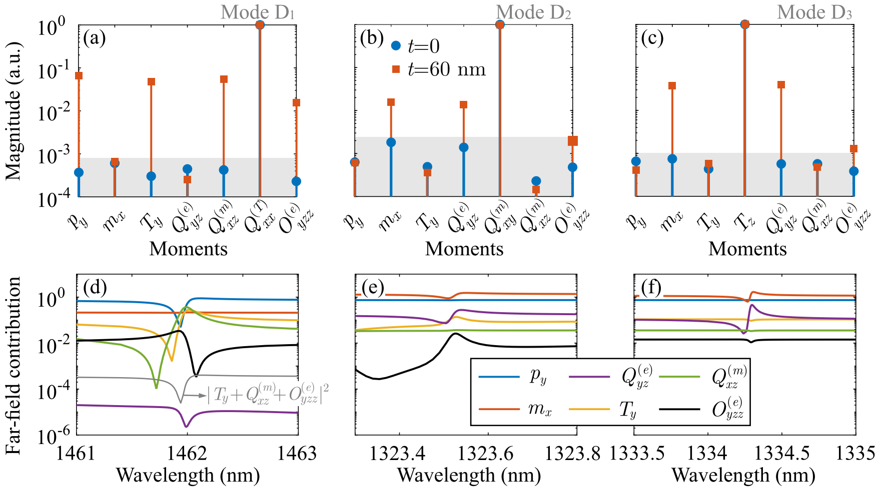

Fig. 5. Multipolar expansion analysis showcasing the transformation of the modes D_1, D_2, and D_3 from BICs to qBICs, as the symmetry of the metasurface is reduced with the introduction of the silicon bridge. (a–c) Analysis with the eigenvector of the three modes. The magnitude of the bright moments coupled to radiation fields polarized in the y direction is depicted, in the case of the symmetric (blue circles), and asymmetric (red squares) metasurface. The bright moments' magnitude in each panel is normalized with respect to the magnitude of the corresponding mode's dark dominant moment, which does not radiate in the far-field. The shaded area marks a practically zero level for the moments' magnitude. (d–f) Normalized far-field contribution of each bright moment individually in the scattered field as a function of the wavelength, when the metasurface is vertically illuminated by a plane wave polarized in the y direction.

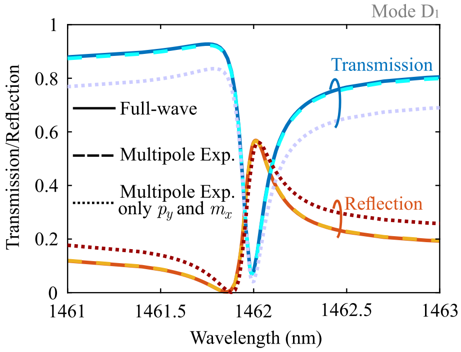

Fig. 6. Transmission and reflection spectra in the vicinity of the qBIC D_1 evaluated directly by plane-wave scattering simulations (solid lines), by the reconstructed scattered field using the contribution of all bright moments (dashed lines), by the reconstructed scattered field using only the contribution of the electric dipole p_y and the magnetic dipole m_x moments (dotted lines).

conclusions are drawn for the rest of the supported modes. To further showcase that the far-field scattering spectrum in the vicinity of the resonance D_1 is predominantly dictated by the moments p_y (resonant contribution) and m_x (non-resonant/background contribution), in Fig. 6 we present the reconstructed transmission and reflection spectra using only the contribution of these two moments (dotted lines), which reproduce fairly accurate the overall transmission and reflection spectra. Therefore, the toroidal quadrupole mode D_1 is transformed into a qBIC by acquiring a significant electric dipole moment p_y which, in turn, is coupled to radiation fields in the normal direction and results in a finite-valued quality factor.

Similar studies are performed for the modes D_2 and D_3 in Fig. 5(b) and (c), respectively. We see that $Q_{xy}^{(m)}$ and T_z remain the dominant moments for the modes D_2 and D_3, respectively, despite the introduction of the asymmetry. The coupling of the two qBICs to the radiation fields in the normal direction is now mediated by the magnetic dipole m_x and the electric quadrupole $Q_{yz}^{(e)}$, which are the moments that increase substantially when the symmetry of the metasurface is reduced. This is also verified in Fig. 5(e) and (f), where the far-field contribution of each moment individually is depicted in the vicinity of the two resonances, when the metasurface is excited by normally incident light polarized in the y direction. Notice also that the electric dipole p_y quantifies only non-resonant contributions. In Fig. 5(d–f) we have allowed for a small imaginary part in silicon's relative permittivity by setting $\gamma = 10^{12}\ \mathrm{s}^{-1}$. This broadens the resonances, enhancing the clarity of the presented results. This adjustment, however, has no impact on the results discussed previously.

As stated above, the qBIC D_4 can only be coupled to the radiation fields polarized in the x direction. As such, one has to examine how the magnitude of the bright moments p_x, m_y, T_x, $Q_{xz}^{(e)}$, $Q_{yz}^{(m)}$, and $O_{xzz}^{(e)}$ changes with the introduction of the asymmetry; the moments $Q_{xz}^{(T)}$ and $O_{yzz}^{(m)}$ are omitted as being negligible. Notice that these moments are different than those studied previously for the modes D_1, D_2, and D_3. This aspect indicates an alternative way in order to determine which polarization excites each mode, i.e., by identifying if the symmetry reduction affects the bright moments coupled to x- or y-polarized radiation fields. In Fig. 7(a), the magnitude of the previously said moments is presented in the case of the symmetric and asymmetric metasurface. Each bright moment's magnitude is normalized, once again, with the dominant dark moment's magnitude, i.e., $Q_{xy}^{(e)}$. It is evident that with the introduction of the silicon bridge, the mode D_4 acquires substantially strong p_x, T_x, $Q_{yz}^{(m)}$, and $O_{xzz}^{(e)}$ moments. However, the moments T_x, $Q_{yz}^{(m)}$, and $O_{xzz}^{(e)}$ almost fully cancel each other out [Fig. 7(b)], leaving the far-field properties of the mode to be predominantly determined by the electric dipole p_x. In Fig. 7(b) we have used $\gamma = 10^{10}\ \mathrm{s}^{-1}$ in the formula of $\varepsilon_{r,\mathrm{Si}}$ in order to broaden the Fano lineshapes and enhance the clarity of the presented results.

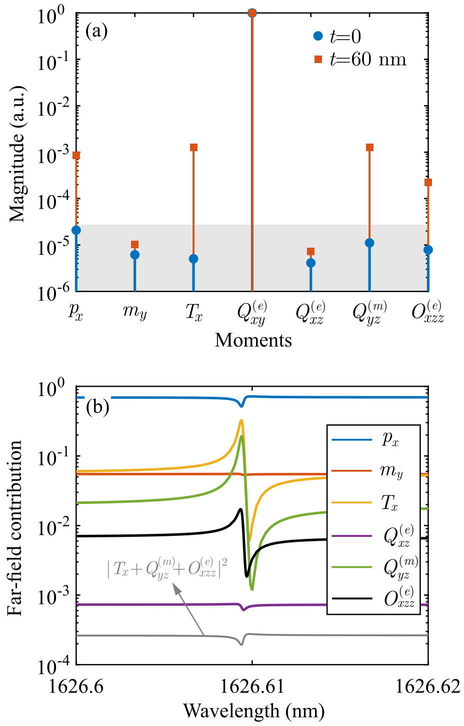

Fig. 7. Multipolar expansion analysis showcasing the transformation of the mode D_4 from BIC to qBIC, as the symmetry of the metasurface is reduced with the introduction of the silicon bridge. (a) Analysis with the eigenvector. The magnitude of the bright moments coupled to radiation fields polarized in the x direction is depicted, in the case of the symmetric (blue circles), and asymmetric (red squares) metasurface. The bright moments' magnitude are normalized with respect to the magnitude of the dominant dark moment $Q_{xy}^{(e)}$, which does not radiate in the far-field in the normal direction. The shaded area marks a practically zero level for the moments' magnitude. (b) Normalized far-field contribution of each bright moment individually in the scattered field as a function of the wavelength, when the metasurface is vertically illuminated by a plane wave polarized in the x direction.

The previous analysis has shown that the four modes under study are transformed from BICs to qBICs by acquiring a radiative/bright moment superimposed onto the dominant dark moment. Concurrently, it has revealed the far-field properties of the four qBICs. Notably, although the near-field profiles of D_1, D_2, D_3, and D_4 are higher-order multipoles (i.e., toroidal quadrupole, magnetic quadrupole, toroidal dipole, and electric quadrupole, respectively), their far-field properties are predominantly dictated by in-plane electric or magnetic dipoles, while the impact of a bright electric quadrupole term is also equally important for the modes D_2 and D_3.

2.3. *Plane-wave scattering analysis*

It is also important to evaluate the transmission spectrum of the investigated metasurface for both $t = 0$ and $t = 60$ nm. This is done by conducting plane-wave scattering simulations with COMSOL Multiphysics®. In Fig. 8(a), the transmission coefficient (black line) is plotted as a function of the wavelength when the symmetric metasurface is vertically illuminated by a plane wave; the result is the same regardless of the polarization of the incident wave. Only the broad (low quality-factor) bright modes B_1, B_2, and B_3 are excited, as they are all clearly marked. The position of the dips in Fig. 8(a) are in excellent agreement with the extracted resonance wavelengths of the bright modes (cf. Table 1). The transmission spectrum also exhibits a peak at $\lambda = n_s\Lambda = 1461.6$ nm, which is attributed to Wood's anomaly (WA), i.e.,

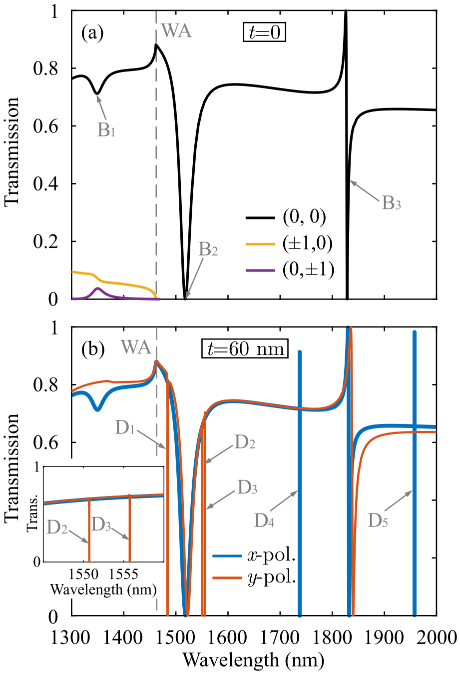

Fig. 8. (a) Transmission spectrum of the symmetric ($t = 0$) metasurface under vertical illumination by a plane wave. The excited bright modes B_1, B_2, and B_3 are clearly marked. The transmission spectrum of higher diffraction orders (yellow and purple curves) is also depicted. (b) Transmission spectrum of the asymmetric ($t = 60$ nm) metasurface under vertical excitation with a plane wave polarized in the x (blue curve) and y (red curve) direction, respectively. With y−polarized incident light the qBICs D_1, D_2, and D_3 are excited, while the x−polarized illumination excites the qBICs D_4 and D_5. Inset: zoomed-in view around $\lambda \sim 1550$ nm, where the resonances D_2 and D_3 are located.

an abrupt redistribution of energy as higher diffraction orders become propagating. Indeed, for $\lambda < 1461.6$ nm, the modes $(\pm 1, 0)$ and $(0, \pm 1)$ become propagating with their transmission coefficients presented in Fig. 8(a) with yellow and purple curves, respectively. The transmission spectrum for the asymmetric metasurface is given in Fig. 8(b). Now the high quality-factor qBICs are also excited, albeit each of them for different polarization of the incident light, i.e., the modes D_1, D_2, and D_3 for y-polarized light, while the modes D_4 and D_5 for x-polarized light. In addition, the degeneracy of the bright modes B_2 and B_3 is also lifted with the introduction of the silicon bridge, rendering the transmission spectrum for x-polarized incident light (blue curve) substantially different than that with y-polarized illumination (red curve). Once again, all the dips in Fig. 8(b) are in excellent agreement with the resonance wavelengths of the modes (cf. Table 1).

3. Experimental demonstration

To corroborate the theoretical studies of Section 2 and verify the existence of the investigated qBICs, we fabricated the square slot metasurface using the procedure described in Ref. [6]. The fabrication was carried out in the fabrication facilities at SiPhotonIC ApS. The metasurface under study was realized on a silicon-on-sapphire platform with a 200 nm silicon layer epitaxially grown on a 430 μm sapphire substrate. The nanoslots were defined by EBL using CSAR e-beam resist and the JBX-9500FSZ 100 kV e-beam writer. After EBL, the STS ICP advanced silicon etcher (ASE) was applied to etch the silicon based on the Bosch etching process, which includes an etching phase with SF_6 and O_2 that alternates with a passivation phase with C_4F_8 for each etching cycle. The gas flow, chamber pressure, platen and coil RF powers were tuned to achieve a vertical etching profile, with almost complete etching of the silicon layer down to the sapphire substrate. After etching, the residual e-beam resist was removed by oxygen plasma cleaning. The dimensions of all metasurface samples were $0.3 \times 0.3\ \mathrm{mm}^2$. A scanning electron microscope (SEM) image of the asymmetric ($t = 60$ nm) and symmetric ($t = 0$) metasurface is presented in Fig. 9(a) and in the inset of Fig. 9(b), respectively. SEM characterization of the square-slotted specimens (both symmetric and asymmetric) was conducted using a Zeiss Gemini 460 (2) field emission scanning electron microscope (FE-SEM) under high vacuum conditions. To suppress high-frequency noise and improve signal-to-noise ratio, frame integration was utilized during scanning. Final images were produced by averaging a minimum of five sequential frames per field of view.

The transmission spectrum of the fabricated samples was measured under normal incidence of a polarized light beam using a Fourier-transform spectrometer (Bruker IFS66) with a spectral resolution of 0.25 pm ($1\ \mathrm{cm}^{-1}$). The light beam from the spectrometer was focused on the sample surface with an Al off-axis parabolic mirror to a spot-size diameter of 100 μm, with an angular spread of ±0.5°. A liquid-nitrogen-cooled InSb photodiode was used as the detector. The results are presented in Fig. 9(b) and (c) for the symmetric metasurface with $t = 0$ (blue curve) and the asymmetric one with $t = 60$ nm (red curve). The experimentally measured spectra are generally in quite good agreement with the theoretically evaluated ones [Fig. 8]. The observed relatively low contrast of the experimentally measured transmission spectrum is attributed to the non-critical coupling to the target qBIC modes. Notably, in the symmetric metasurface ($t = 0$) apart from the bright modes B_1, B_2 and B_3, the dark modes D_1, D_2 and D_4 are also excited. This can be attributed to (i) the stochastic variation of the geometric parameters of the meta-atoms over the entire extent of the metasurface, as thoroughly explained in Ref. [6], (ii) the finite angular content of the illuminating beam, and (iii) the finite extent of the fabricated metasurface samples. Note that an obliquely incident light beam effectively reduces the symmetry of the metasurface facilitating the coupling of the dark modes to the radiation fields in the corresponding direction [25,27,28,31]. On the contrary, the mode D_3 is solely excited when $t = 60$ nm [Fig. 9(b) and (c)]. Additionally, the observed rippling in the transmission spectra of Fig. 9(b) and (c) is due to the underlying Fabry–Perot resonances in the 430 μm sapphire substrate [6,40,41]. The latter are characterized by a free-spectral range (FSR) of $\mathrm{FSR} = \lambda^2/(2n_s h_s) \sim 1.82$ nm, where h_s is the height of the sapphire substrate and $\lambda = 1650$ nm (mid-wavelength in the range 1300–2000 nm).

To assess the experimentally obtained quality factors of the Mie modes supported by the asymmetric metasurface ($t = 60$ nm), we fit the measured transmission spectrum in the vicinity of each mode with a closed-form Fano transmission relation [30,31]. The Fabry–Perot-oriented rippling can also be considered through an Airy distribution superimposed onto the Fano function [6]. The fitted spectrum for the mode D_1 is presented in Fig. 9(d), where an experimentally obtained quality factor of $Q = 840$ is extracted. The corresponding quality factors for the modes D_2, D_3, and D_4 are $Q = 700$, $Q = 850$, and $Q = 270$, respectively. It is evident that the experimentally obtained quality factors are substantially lower in comparison to those theoretically evaluated in Section 2 [cf. Table 1], which only take into account radiation losses. This significant difference is mainly attributed to the statistical variation of the geometric parameters over the extent of the fabricated metasurface samples [6,42]. In particular, the slot width s is the parameter that mainly affects the resonance wavelengths of the investigated qBICs. Based on a set of SEM images, such as the one shown in Fig. 9(a), an analysis has been performed on the statistical distribution of the slot width s over large surface areas of the fabricated metasurface samples. The image processing is performed in Python: first, the SEM images were imported as an array of greyscale tones $T(x, y)$. Then, the slot width is estimated by taking straight lines over the image, calculating the greyscale profiles, and setting a threshold value so as to clearly identify silicon from slotted air regions [6]. The histogram of the variation of s is depicted in Fig. 10(a), and a standard deviation of $\sigma = 2.5$ nm

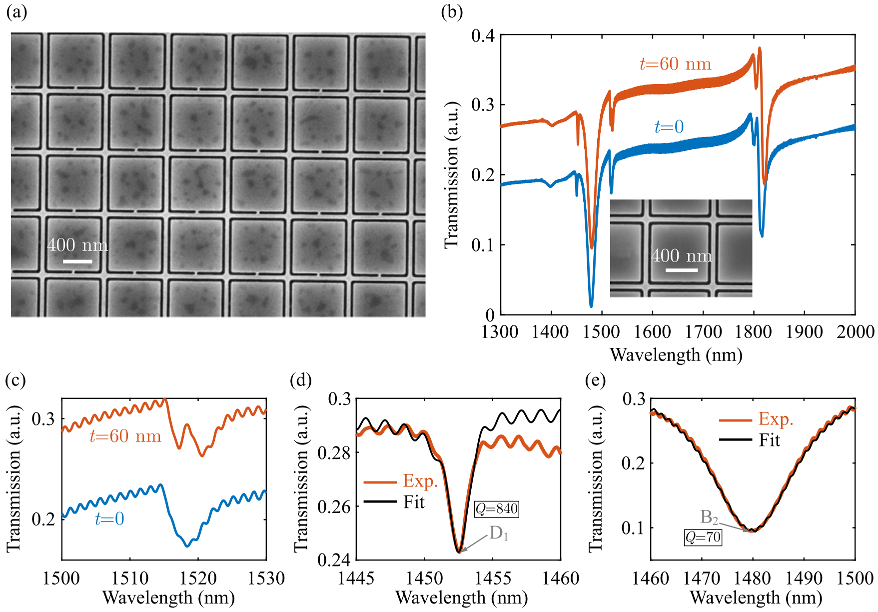

Fig. 9. Experimental study of the silicon slot metasurface. (a) SEM image of the asymmetric structure (t = 60 nm). (b) Experimentally measured transmission spectra for the symmetric (t = 0) and asymmetric (t = 60 nm) metasurface. Inset: SEM image of the symmetric metasurface. (c) Zoomed-in view of (b) around $\lambda \sim 1520$ nm, where the resonances D_2 and D_3 are located. (d) and (e) Fit of the transmission spectrum with a closed-form Fano transmission relation in the vicinity of the resonances (d) D_1, and (e) B_2 revealing the experimentally obtained quality factor of the two modes.

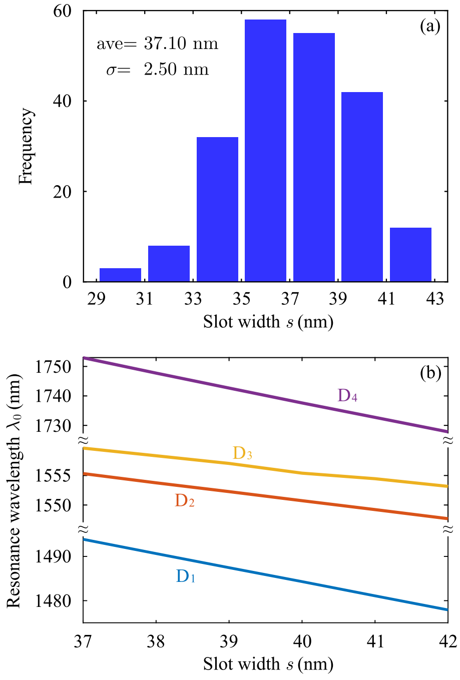

Fig. 10. (a) Histogram showing the statistical variation of the slot width s over the entire extent of the fabricated metasurface. (b) Resonance wavelengths of the qBICs D_1, D_2, D_3, and D_4 as a function of the slot width s of the metasurface. For every value of s, the inner separation of slots w changes appropriately so that the pitch remains constant to $\Lambda = 840$ nm.

is thereafter extracted. Although it may at first seem unimportant, such deviations from the nominal value of $s = 40$ nm result in a significant shifting of many nanometers in the resonance wavelengths of all four qBICs [Fig. 10(b)]. Hence, the stochastic variation of s not only explains the large difference between theoretical and experimental quality factors, but also the fact that some of the dark resonances are excited even in the symmetric metasurface, as mentioned above. The fabrication-related-imperfections introducing additional absorptive and scattering losses at the sidewalls of the etched silicon slots are also expected to play a role, though of lesser importance, in lowering the quality factors of the qBICs [42]. On the contrary, the experimentally attained quality factor of the bright mode B_2 is $Q = 70$ [Fig. 8(e)]. This value is practically identical to the theoretically evaluated one [cf. Table 1], which implies that the radiative dissipation is the dominant loss channel for the mode B_2. Despite the substantial resonance damping/broadening of the investigated qBICs, the previously presented experimental studies have undoudebtly confirmed the existence of the quasi-dark states in the silicon square slot metasurface under consideration.

4. Discussion: lasing and nonlinear applications

The rich variety of qBIC states studied previously renders the investigated metasurface an excellent platform for several lasing and nonlinear applications. More specifically, silicon has a substantially strong Kerr effect with a nonlinear refractive index of $n_2 \approx 2.5 \times 10^{-18}$ $\mathrm{m^2/W}$ in the wavelength range of interest. To quantify the suitability of the qBICs D_1, D_2, D_3, and D_4 for nonlinear applications, we evaluate the self-phase modulation (SPM) parameter. It is given by [43]

$$\gamma_{\mathrm{SPM}} = \frac{1}{12}\omega_0 c_0 \varepsilon_0 \varepsilon_{r,\mathrm{Si}} n_{2,\mathrm{Si}} \iiint_{V_{\mathrm{Si}}} \left[2|\mathbf{E}_{\mathrm{ref}}|^4 + |\mathbf{E}_{\mathrm{ref}} \cdot \mathbf{E}_{\mathrm{ref}}|^2\right] \mathrm{d}V, \tag{1}$$

where $\mathbf{E}_{\mathrm{ref}}$ is the normalized eigenvector of each mode in order to have energy equal to one [44], ω_0 the resonance frequency, c_0 the speed of light in vacuum, and ε_0 the vacuum permittivity. The integration is conducted over the volume of the unit cell occupied by silicon. The γ_{SPM} parameter essentially describes the degree of overlap between the optical mode and the nonlinear material and can be viewed as an inversely proportional quantity to the effective modal volume. Hence, it constitutes an indicative metric for the nonlinear response of each mode, despite the fact that other parametric processes stemming from the Kerr effect, such as THG and DFWM, are described by slightly different nonlinear parameters [43].

The obtained γ_{SPM} parameters for the investigated qBICs are summarized in Table 2. For ease of comparison, the corresponding quantity

Table 2
Nonlinear and lasing metrics for the qBICs D_1, D_2, D_3, and D_4, as well as the bright mode B_2.

Metric	D_1	D_2	D_3	D_4	B_2
γ_{SPM} $(\mathrm{W}^{-1}\mathrm{s}^{-2})$	9.2×10^{23}	1.39×10^{23}	1.33×10^{23}	2.89×10^{23}	5×10^{22}
ξ_g $(\mathrm{V\,C}^{-1}\mathrm{m})$	1.07×10^{9}	4.92×10^{8}	4.46×10^{8}	4.51×10^{9}	8.88×10^{8}
$Q\,\xi_g$ $(\mathrm{V\,C}^{-1}\mathrm{m})$	3×10^{13}	8.9×10^{13}	1.92×10^{14}	4.38×10^{15}	1.13×10^{11}

of the bright mode B_2 in the symmetric metasurface ($t = 0$) is also included. We see that the mode D_1 has the greatest γ_{SPM} parameter, rendering it the most favorable for nonlinear applications. The rest of qBICs also exhibit high nonlinear parameters, which are one order of magnitude greater than that of the leaky mode B_2, thus, highlighting the strong field confinement offered by the qBICs. To further highlight the superiority of the qBIC D_1 for nonlinear applications, we introduce the characteristic power density, I_{SPM}, which constitutes an estimate of the irradiance needed for the SPM effect to manifest. It is given by $I_{\mathrm{SPM}} = P_{\mathrm{SPM}}/\Lambda^2$, where $P_{\mathrm{SPM}} = \tau^{-2}\gamma_{\mathrm{SPM}}^{-1}$ is the characteristic power per unit cell, with $\tau = 2Q/\omega_0$ the cavity lifetime [43]. Using the experimentally attained quality factors, we obtain $I_{\mathrm{SPM}} = 88\ \mathrm{MW/cm^2}$ for the mode D_1, with the I_{SPM} values for the modes D_2, D_3 and D_4 being at least one order of magnitude higher. Specifically, we have $I_{\mathrm{SPM}} = 768\ \mathrm{MW/cm^2}$, $I_{\mathrm{SPM}} = 541\ \mathrm{MW/cm^2}$, and $I_{\mathrm{SPM}} = 2\ \mathrm{GW/cm^2}$ for D_2, D_3, and D_4, respectively. Among the various nonlinear applications, highly efficient THG and HHG attract great scientific attention, as they enable access to spectral regions, such as the UV, where lasing sources are scarce. Therefore, the mode D_1 can be readily used as the pump mode excited at the fundamental frequency and resulting in a substantial enhancement of the conversion efficiency of the parametric processes [19,22,23]. Alternatively, the modes D_1 and D_3 having the lowest I_{SPM} parameters, can be simultaneously utilized in a control-probe scheme, where the strong control mode generates the nonlinearity that affects the weak probe mode, thus, achieving low-power all-optical control of light.

The silicon square slot metasurface under study is also highly favorable for lasing applications. The gain mechanism can be provided by organic dye molecules hosted in a polymer, such as poly(methyl methacrylate) (PMMA), filling the slot. Such metasurface lasing elements are at the forefront of scientific research [26–28] leveraging the well-researched and mature technology of optically pumped organic dye solutions. Specifically, for the wavelength range of interest ($\lambda = 1300$–2000 nm), the dye IR26 can be utilized [45]. The metric that quantifies the strength of each mode for light-emitting applications is the overlap factor [44]

$$\xi_g = \frac{1}{4}\iiint_{V_{\mathrm{slot}}} |\mathbf{E}_{\mathrm{ref}}|^2\,\mathrm{d}V. \tag{2}$$

where the integration is now conducted over the volume of the unit cell occupied by the slot (filled by the gain medium). The modal properties of the four qBICs have been recalculated through eigenfrequency simulations for the case where the polymer occupying the slot has an index of $n = 1.5$. The presence of the polymer redshifts the resonance wavelengths by 10–15 nm for the modes D_1, D_2, and D_3, while their quality factors are substantially increased. On the contrary, the resonance wavelength of the mode D_4 redshifts by ~ 130 nm and its quality factor decreases considerably. The obtained values of ξ_g for the investigated qBICs and the bright mode B_2 are presented in Table 2. The qBIC D_4 exhibits by far the largest ξ_g parameter, since it is mainly concentrated inside the slot [see Fig. 2(d)]. The mode D_1 has the second highest ξ_g parameter followed by the modes D_2 and D_3. Surprisingly, the bright mode B_2 has a comparably high ξ_g with those of D_2 and D_3, but its very low quality factor would prohibit lasing. To support this claim, in Table 2 we also compile the quantity $Q\,\xi_g$, which is inversely proportional to the lasing threshold [44]; we use the Q values that have been theoretically evaluated when the slot is filled with the polymer. The mode D_4 is also characterized by the highest $Q\,\xi_g$ entity, due to its both high field-concentration in the slot and ultrahigh quality factor. Consequently, this could lead to an ultralow lasing threshold when the qBIC D_4 is exploited as the lasing mode. Notice that the leaky mode B_2 has at least two orders of magnitude lower $Q\,\xi_g$ value in comparison to those of the four qBICs. In a different approach, the qBICs D_2 and D_3 can be utilized in a dual-mode lasing scheme [27,28], since they have (i) identical far-field properties, (ii) close resonance wavelengths, and (iii) similar quality factors.

5. Conclusion

To recapitulate, we have studied both theoretically and experimentally a novel silicon square slot metasurface hosting a rich variety of BICs including the intricate toroidal dipole and toroidal quadrupole. By appropriately reducing the symmetry of the metasurface, the symmetry-protected modes are coupled to radiation fields in the normal direction. The modal properties of the qBICs, such as their quality factors, as well as their near- and far-field properties, have been thoroughly assessed using a variety of theoretical tools. The latter includes an auxiliary-fields eigenfrequency formulation taking accurately into account the dispersion of silicon, and multipole expansion analysis unraveling the physical processes governing the transformation of the dark resonances to quasi-dark ones. Notably, our analysis has revealed that the investigated qBICs radiate in the far-field as simple in-plane electric or magnetic dipoles, despite the fact that their near-field profiles are those of higher-order multipoles. The presence of the qBICs under study has been experimentally confirmed by measuring the transmission spectrum of the metasurface fabricated through EBL and ICP etching. Overall, the distinct field distributions of the supported qBICs enable their use for different applications. Specifically, the toroidal quadrupole mode is more favorable for nonlinear applications stemming from silicon's Kerr effect, such as THG, while the electric quadrupole mode is advantageous for lasing applications when organic dye media are appropriately integrated into the structure. The toroidal dipole and magnetic quadrupole modes are promising for dual-mode lasing operation.

CRediT authorship contribution statement

G. Nousios: Writing – original draft, Visualization, Software, Methodology, Formal analysis, Conceptualization. **J.F. Algorri:** Writing – review & editing, Methodology, Conceptualization. **W. Fuscaldo:** Writing – review & editing, Methodology. **F. Dell'Olio:** Writing – review & editing, Conceptualization. **S. Romano:** Resources, Investigation. **G. Zito:** Resources, Investigation. **B. Miranda:** Resources, Investigation. **Y. Ding:** Writing – review & editing, Resources, Investigation. **V. Dmitriev:** Writing – review & editing, Formal analysis. **L.C. Andreani:** Writing – review & editing, Supervision, Software, Resources, Formal analysis, Data curation. **M. Galli:** Writing – review & editing, Resources, Investigation. **O. Tsilipakos:** Writing – review & editing, Supervision, Methodology, Formal analysis, Conceptualization. **E.E. Kriezis:** Writing – review & editing, Supervision, Methodology, Formal analysis, Conceptualization. **D.C. Zografopoulos:** Writing – review & editing, Supervision, Project administration, Methodology, Funding acquisition, Formal analysis, Data curation, Conceptualization.

Declaration of competing interest

The authors declare that they have no known competing financial interests or personal relationships that could have appeared to influence the work reported in this paper.

Acknowledgment

This research work is supported by the project PRIN-2022 ALPHA "ALl-dielectric resonant metasurfaces enhancing PHoton emission phenomenA” (CUP:D53D23001060006) funded by the Italian Ministry of University and Research.

Data availability

Data will be made available on request.

References

[1] S.B. Glybovski, S.A. Tretyakov, P.A. Belov, Y.S. Kivshar, C.R. Simovski, Metasurfaces: from microwaves to visible, Phys. Rep. 634 (2016) 1–72, https://doi.org/10.1016/j.physrep.2016.04.004

[2] T. Liu, R. Xu, P. Yu, Z. Wang, J. Takahara, Multipole and multimode engineering in mie resonance-based metastructures, Nanophotonics 9 (5) (2020) 1115–1137, https://doi.org/10.1515/nanoph-2019-0505

[3] X. Luo, X. Du, R. Huang, G. Li, High-Q and strong chiroptical responses in planar metasurfaces empowered by Mie surface lattice resonances, Laser Photon. Rev. 17 (10) (2023) 2300186, https://doi.org/10.1002/lpor.202300186

[4] M.-C. Cho, K.-H. Kim, Efficient frequency conversion in dielectric metasurfaces supporting both surface lattice resonances and quasi-bound states in the continuum, Optics. Laser. Technol. 180 (2025) 111545, https://doi.org/10.1016/j.optlastec.2024.111545

[5] O. Tsilipakos, A.C. Tasolamprou, T. Koschny, M. Kafesaki, E.N. Economou, C.M. Soukoulis, Pairing toroidal and magnetic dipole resonances in elliptic dielectric rod metasurfaces for reconfigurable wavefront manipulation in reflection, Adv. Optical Mater. 6 (22) (2018) 1800633, https://doi.org/10.1002/adom.201800633

[6] J.F. Algorri, F. Dell’Olio, Y. Ding, F. Labbé, V. Dmitriev, J.M. López-Higuera, J.M. Sánchez-Pena, L.C. Andreani, M. Galli, D.C. Zografopoulos, Experimental demonstration of a silicon-slot quasi-bound state in the continuum in near-infrared all-dielectric metasurfaces, Optics. Laser. Technol. 161 (January) (2023) 109199, https://doi.org/10.1016/j.optlastec.2023.109199

[7] D.C. Zografopoulos, V. Dmitriev, Quasi-dark resonances in silicon metasurface for refractometric sensing and tunable notch filtering, J. Lightwave Technol. 39 (21) (2021) 6985–6993, https://doi.org/10.1109/jlt.2021.3107953

[8] Y. Zhang, Y. Chen, T. Wang, Q. Zhu, M. Gu, Ultrahigh performance passive radiative cooling by hybrid polar dielectric metasurface thermal emitters, Opto-Electron. Adv. 7 (4) (2024) 230194, https://doi.org/10.29026/oea.2024.230194

[9] T. Nan, H. Zhao, J. Guo, X. Wang, H. Tian, Y. Zhang, Generation of structured light beams with polarization variation along arbitrary spatial trajectories using tri-layer metasurfaces, Opto-Electron. Sci. 3 (5) (2024) 230052, https://doi.org/10.29026/oes.2024.230052

[10] H. Pan, M.K. Chen, D.P. Tsai, S. Wang, Nonreciprocal pancharatnam-berry metasurface for unidirectional wavefront manipulations, Opt. Express. 32 (15) (2024) 25632–25643, https://doi.org/10.1364/OE.525690

[11] C.W. Hsu, B. Zhen, A.D. Stone, J.D. Joannopoulos, M. Soljačić, Bound states in the continuum, Nat. Rev. Mater. 1 (9) (2016) 16048, https://doi.org/10.1038/natrevmats.2016.48

[12] T. Shi, Z.-L. Deng, Q.-A. Tu, Y. Cao, X. Li, Displacement-mediated bound states in the continuum in all-dielectric superlattice metasurfaces, PhotoniX 2 (1) (2021) 7, https://doi.org/10.1186/s43074-021-00029-x

[13] T. Shi, Z.-L. Deng, G. Geng, X. Zeng, Y. Zeng, G. Hu, A. Overvig, J. Li, C.-W. Qiu, A. Alù, Y.S. Kivshar, X. Li, Planar chiral metasurfaces with maximal and tunable chiroptical response driven by bound states in the continuum, Nat. Commun. 13 (1) (2022) 4111, https://doi.org/10.1038/s41467-022-31877-1

[14] Z.-L. Deng, F.-J. Li, H. Li, X. Li, A. Alù, Extreme diffraction control in metagratings leveraging bound states in the continuum and exceptional points, Laser Photon. Rev. 16 (6) (2022) 2100617, https://doi.org/10.1002/lpor.202100617

[15] Z. Feng, T. Shi, G. Geng, J. Li, Z.-L. Deng, Y. Kivshar, X. Li, Dual-band polarized upconversion photoluminescence enhanced by resonant dielectric metasurfaces, eLight 3 (1) (2023) 21, https://doi.org/10.1186/s43593-023-00054-2

[16] L. Huang, L. Xu, D.A. Powell, W.J. Padilla, A.E. Miroshnichenko, Resonant leaky modes in all-dielectric metasystems: fundamentals and applications, Phys. Rep. 1008 (2023) 1–66, https://doi.org/10.1016/j.physrep.2023.01.001

[17] D.C. Zografopoulos, O. Tsilipakos, Recent advances in strongly resonant and gradient all-dielectric metasurfaces, Mater. Adv. 4 (1) (2023) 11–34, https://doi.org/10.1039/d2ma00910h

[18] S. Campione, S. Liu, L. I. Basilio, L. K. Warne, W. L. Langston, T. S. Luk, J. R. Wendt, J. L. Reno, G. A. Keeler, I. Brener, M. B. Sinclair, Broken symmetry dielectric resonators for high quality factor fano metasurfaces, ACS Photonics 3 (12) (2016) 2362–2367. arXiv:1607.06469, https://doi.org/10.1021/acsphotonics.6b00556

[19] K. Koshelev, Y. Tang, K. Li, D. Y. Choi, G. Li, Y. Kivshar, Nonlinear metasurfaces governed by bound states in the continuum, ACS Photonics 6 (7) (2019) 1639–1644. arXiv:1905.05402, https://doi.org/10.1021/acsphotonics.9b00700

[20] Z. Liu, Y. Xu, Y. Lin, J. Xiang, T. Feng, Q. Cao, J. Li, S. Lan, J. Liu, High-Q quasibound states in the continuum for nonlinear metasurfaces, Phys. Rev. Lett. 123 (25) (2019) 253901, https://doi.org/10.1103/PhysRevLett.123.253901

[21] L. Xu, K.Z. Kamali, L. Huang, M. Rahmani, A. Smirnov, R. Camacho-Morales, Y. Ma, G. Zhang, M. Woolley, D. Neshev, A.E. Miroshnichenko, Dynamic nonlinear image tuning through magnetic dipole quasi-BIC ultrathin resonators, Adv. Sci. 6 (15) (2019) 1802119, https://doi.org/10.1002/advs.201802119

[22] S. Xiao, M. Qin, J. Duan, T. Liu, Robust enhancement of high-harmonic generation from all-dielectric metasurfaces enabled by polarization-insensitive bound states in the continuum, Opt. Express 30 (18) (2022) 32590. arXiv:2203.10226, https://doi.org/10.1364/oe.468925

[23] G. Zograf, K. Koshelev, A. Zalogina, V. Korolev, R. Hollinger, D.Y. Choi, M. Zuerch, C. Spielmann, B. Luther-Davies, D. Kartashov, S.V. Makarov, S.S. Kruk, Y. Kivshar, High-harmonic generation from resonant dielectric metasurfaces empowered by bound states in the continuum, ACS. Photonics 9 (2) (2022) 567–574, https://doi.org/10.1021/acsphotonics.1c01511

[24] S.T. Ha, Y.H. Fu, N.K. Emani, Z. Pan, R.M. Bakker, R. Paniagua-Domínguez, A.I. Kuznetsov, Directional lasing in resonant semiconductor nanoantenna arrays, Nat. Nanotechnol. 13 (11) (2018) 1042–1047, https://doi.org/10.1038/s41565-018-0245-5

[25] M. Wu, S.T. Ha, S. Shendre, E.G. Durmusoglu, W.K. Koh, D.R. Abujetas, J.A. Sánchez-Gil, R. Paniagua-Domínguez, H.V. Demir, A.I. Kuznetsov, Room-temperature lasing in colloidal nanoplatelets via Mie-resonant bound states in the continuum, Nano Lett. 20 (8) (2020) 6005–6011, https://doi.org/10.1021/acs.nanolett.0c01975

[26] J.-H. Yang, Z.-T. Huang, D.N. Maksimov, P.S. Pankin, I.V. Timofeev, K.-B. Hong, H. Li, J.-W. Chen, C.-Y. Hsu, Y.-Y. Liu, T.-C. Lu, T.-R. Lin, C.-S. Yang, K.-P. Chen, Low-threshold bound state in the continuum lasers in hybrid lattice resonance metasurfaces, Laser Photon. Rev. 15 (10) (2021) 2100118, https://doi.org/10.1002/lpor.202100118

[27] S.I. Azzam, K. Chaudhuri, A. Lagutchev, Z. Jacob, Y.L. Kim, V.M. Shalaev, A. Boltasseva, A.V. Kildishev, Single and multi-mode directional lasing from arrays of dielectric nanoresonators, Laser Photon. Rev. 15 (3) (2021) 2000411, https://doi.org/10.1002/lpor.202000411

[28] H. Xue, J. Niu, S. Chen, L. Li, S. Zhao, C. Lu, F. Jin, C. Xie, L. Shi, Low-threshold lasing from bound states in the continuum with dielectric metasurfaces, Optics Lett. 48 (24) (2023) 6480, https://doi.org/10.1364/ol.505704

[29] H. Xue, J. Niu, C. Wang, S. Chen, C. Lu, P. Zhang, F. Jin, C. Xie, L. Shi, Lasing action assisted by bound states in the continuum in a silicon metasurface, Optics. Laser. Technol. 177 (2024) 111103, https://doi.org/10.1016/j.optlastec.2024.111103

[30] J.F. Algorri, F. Dell’Olio, P. Roldán-Varona, L. Rodríguez-Cobo, J.M. López-Higuera, J.M. Sánchez-Pena, D.C. Zografopoulos, Strongly resonant silicon slot metasurfaces with symmetry-protected bound states in the continuum, Opt. Express 29 (7) (2021) 10374–10385, https://doi.org/10.1364/OE.415377

[31] J.F. Algorri, F. Dell’Olio, P. Roldán-Varona, L. Rodríguez-Cobo, J.M. López-Higuera, J.M. Sánchez-Pena, V. Dmitriev, D.C. Zografopoulos, Analogue of electromagnetically induced transparency in square slotted silicon metasurfaces supporting bound states in the continuum, Opt. Express 30 (3) (2022) 4615–4630, https://doi.org/10.1364/OE.446720

[32] W. Yan, R. Faggiani, P. Lalanne, Rigorous modal analysis of plasmonic nanoresonators, Phys. Rev. B. 97 (20) (2018) 205422, https://doi.org/10.1103/PhysRevB.97.205422

[33] T. Christopoulos, E.E. Kriezis, O. Tsilipakos, Multimode non-hermitian framework for third harmonic generation in nonlinear photonic systems comprising two-dimensional materials, Phys. Rev. B. 107 (3) (2023) 035413, https://doi.org/10.1103/PhysRevB.107.035413

[34] V. Savinov, V.A. Fedotov, N.I. Zheludev, Toroidal dipolar excitation and macroscopic electromagnetic properties of metamaterials, Phys. Rev. B. 89 (20) (2014) 205112, https://doi.org/10.1103/PhysRevB.89.205112

[35] T. Christopoulos, O. Tsilipakos, G. Sinatkas, E.E. Kriezis, On the calculation of the quality factor in contemporary photonic resonant structures, Opt. Express 27 (10) (2019) 14505–14522, https://doi.org/10.1364/OE.27.014505

[36] M. Dehmollaian, C. Caloz, General mapping between complex spatial and temporal frequencies by analytical continuation, IEEE Trans. Antennas Propag. 69 (10) (2021) 6531–6545, https://doi.org/10.1109/TAP.2021.3061262

[37] F. Mesa, G. Valerio, R. Rodríguez-Berral, O. Quevedo-Teruel, Simulation-assisted efficient computation of the dispersion diagram of periodic structures: a comprehensive overview with applications to filters, leaky-wave antennas and metasurfaces, IEEE Antennas Propag. Mag. 63 (5) (2021) 33–45, https://doi.org/10.1109/MAP.2020.3003210

[38] K. Koshelev, S. Lepeshov, M. Liu, A. Bogdanov, Y. Kivshar, Asymmetric metasurfaces with high-Q resonances governed by bound states in the continuum, Phys. Rev. Lett. 121 (19) (2018) 193903, https://doi.org/10.1103/PhysRevLett.121.193903

[39] O. Tsilipakos, Z. Viskadourakis, A.C. Tasolamprou, D.C. Zografopoulos, M. Kafesaki, G. Kenanakis, E.N. Economou, Meta-atoms with toroidal topology for strongly resonant responses, Micromachines 14 (2) (2023) 468, https://doi.org/10.3390/mi14020468

[40] M. Lawrence, D.R. Barton, J. Dixon, J.-H. Song, J. van de Groep, M.L. Brongersma, J.A. Dionne, High quality factor phase gradient metasurfaces, Nat. Nanotechnol. 15 (11) (2020) 956–961, https://doi.org/10.1038/s41565-020-0754-x

[41] H. Jiang, Y. Cai, Z. Han, Enhanced high-harmonic generation with spectral tunability in nonlocal metasurfaces enabled by the excitation of quasiguided modes, Phys. Rev. B. 110 (24) (2024) 245424, https://doi.org/10.1103/PhysRevB.110.245424

[42] J. Kühne, J. Wang, T. Weber, L. Kühner, S.A. Maier, A. Tittl, Fabrication robustness in BIC metasurfaces, Nanophotonics 10 (17) (2021) 4305–4312, https://doi.org/10.1515/nanoph-2021-0391

[43] T. Christopoulos, O. Tsilipakos, G. Sinatkas, E.E. Kriezis, Degenerate four-wave mixing in nonlinear resonators comprising two-dimensional materials: a coupled-mode theory approach, Phys. Rev. B. 98 (23) (2018) 235421, https://doi.org/10.1103/PhysRevB.98.235421

[44] G. Nousios, T. Christopoulos, O. Tsilipakos, E.E. Kriezis, Integrated lasers with transition-metal-dichalcogenide heterostructures: analysis and design utilizing coupled-mode theory for two-dimensional materials, Phys. Rev. Appl. 19 (6) (2023) 064027, https://doi.org/10.1103/PhysRevApplied.19.064027

[45] D. Korn, M. Lauermann, S. Koeber, P. Appel, L. Alloatti, R. Palmer, P. Dumon, W. Freude, J. Leuthold, C. Koos, Lasing in silicon-organic hybrid waveguides, Nat. Commun. 7 (1) (2016) 10864, https://doi.org/10.1038/ncomms10864